A New SAR Interferometry Approach to Linear Infrastructure Monitoring using Spatial Displacement Gradients

Andreas Piter[1], Mahmud Haghshenas Haghighi[1], Mahdi Motagh[2,1]

[1] Institute of Photogrammetry and GeoInformation, Leibniz University Hannover, Germany - {piter, mahmud, motagh}@ipi.uni-hannover.de
[2] GFZ Helmholtz Centre for Geosciences, 14473 Potsdam, Germany - mahdi.motagh@gfz.de

Keywords: InSAR, Gradient, Linear Infrastructure, Sentinel-1, TerraSAR-X

Abstract

Monitoring linear infrastructures such as railways and highways with Multitemporal Interferometric Synthetic Aperture Radar (MTInSAR) requires to identify spatial displacement gradients to assess related hazards. Estimating the spatial gradients involves the retrieval of the displacement time series in MTInSAR for coherent pixels. However, the algorithms are computationally expensive because pixels outside the linear infrastructure are processed as they are required to aid the phase unwrapping and atmospheric phase filtering at the linear infrastructure. We propose a new approach which makes use of the known location of the linear infrastructure in the SAR images and estimate the differential displacement velocities along the infrastructure from the wrapped interferometric phases. In this way, the effect of incoherent pixels from outside the linear infrastructure and the potential error propagation during spatial phase unwrapping are mitigated. Our experiments based on TerraSAR-X and Sentinel-1 images show good agreement between the estimated spatial gradient velocities from our method and the conventional MTInSAR results. The sensitivity of the choice of grid size is evident in the resultant Root Mean Square Error (RMSE), which is approximately 0.1 cm/year when compared to the conventional MTInSAR results. This is achieved with a grid size larger than 300 m, which smoothed small variations in the differential velocity. Applying our method on Sentinel-1 images enables computationally efficient monitoring of linear infrastructures exploiting the wide area coverage and availability of the SAR images.

1. Introduction

Multitemporal Interferometric Synthetic Aperture Radar (MTInSAR) has evolved into a powerful tool for observing displacements at the Earth's surface with long time series derived across large areas. The availability of freely available Sentinel-1 images with extensive area coverage and regular acquisitions has fostered the development of ground motion monitoring services (Kalia et al., 2017; Crosetto et al., 2020; Morishita, 2021) in order to assess natural (Gürboğa et al., 2025) and anthropogenic hazards (Haghighi and Motagh, 2024).
While homogeneously subsiding infrastructures are less vulnerable, spatially irregular displacements result in spatial displacement gradients that might lead to damage (Barra et al., 2022). Assessing infrastructure damage risk requires monitoring hazard resulting from deformation. Spatial gradients are usually derived as a product from MTInSAR in a post-processing step. However, the differential displacement velocity between neighbouring points often are an intermediate product during MTInSAR which is used to derive the displacement velocity and the displacement time series (Ferretti et al., 2001; Mora et al., 2003; Van Leijen, 2014). While the displacement time series is valuable to assess hazards resulting from acceleration of the displacement, it is discarded for the assessment of the spatial gradient velocities which is commonly computed from the mean displacement velocities.
Monitoring linear infrastructures, such as railways and highways, benefits from the spatial coverage of Sentinel-1 images due to their elongated shape that covers hundreds of kilometers. However, the narrow shape of the linear infrastructure typically with a width of up to 40 m poses challenges for the MTInSAR processing (Piter et al., 2024), for which the method underlying a generic ground motion service is not tailored to. The number of coherent pixels at the linear infrastructure derived from Sentinel-1 images is limited and the pixel's distribution is heterogeneous as a consequence of the sensor's medium spatial resolution of 5 m×20 m in range and azimuth, respectively. For assessing the displacement at the linear infrastructure, the majority of the pixels which are processed with MTInSAR methods is not intersecting the object and thus is not relevant for the application. Nevertheless, the displacement is often derived for the surrounding area to capture hazards from e.g. landslides (Raspini et al., 2019). The pixels outside the transport infrastructure are needed to estimate and remove the atmospheric effect which is the biggest error source in MTInSAR (Hanssen, 2001). Considering the large area that needs to be processed with MTInSAR to monitor the whole linear infrastructure, the pixels outside the object limit the processing in two ways. On the one hand, the large number of pixels demands high computational resources for phase unwrapping and atmospheric filtering. On the other hand, phase unwrapping errors can be caused by noise in pixels outside the linear infrastructure and will be propagated, which could, however, be avoided by reducing the processing to pixels at the linear infrastructure itself. For this reason, national ground motion services are often not ideal for the transport infrastructure monitoring task. In this paper, we aim at addressing these two major challenges.

We propose a new concept for linear infrastructure monitoring using MTInSAR which considers the shape of the infrastructure. The novelty of our work is the preselection of pixels at the linear infrastructure in combination with the estimation of the spatial displacement gradients along the linear infrastructure from the wrapped interferometric phases. The approach comes with computational efficiency, reduces the impact of phase unwrapping errors and does not require atmospheric filtering. The rest of the paper is structured as follows. First, we review the lit-

This contribution has been peer-reviewed. The double-blind peer-review was conducted on the basis of the full paper.
https://doi.org/10.5194/isprs-annals-XI-3-2026-447-2026 | © Author(s) 2026. CC BY 4.0 License.

erature about infrastructure monitoring and gradient estimation. Second, we present our new gradient-based method. Third, we demonstrate the performance of the method with a case study. Finally we conclude our work.

2. Literature Review

For monitoring of linear infrastructures, such as highways and railways, often off-the-shelf MTInSAR methods have been used to derive displacement (Chang and Hanssen, 2015; Orellana et al., 2020; Bernhard et al., 2024). A few works have concentrated on the methodological improvements to MTInSAR for linear infrastructures. For example, MTInSAR methods have been tailored to highways and railways including performance assessment of different pixel selection techniques (Piter et al., 2024) and a relaxed threshold was proposed for pixels on the linear infrastructure to increase the pixel density at the object (Macchiarulo et al., 2022). In the postprocessing step, i.e. after the displacement retrieval, the geolocation accuracy of Point Scatterer (PS) pixels can be improved by combining the MTInSAR results with laser scanning measurements (Chang et al., 2020). To improve the interpretability of the displacement results, the Line-of-Sight (LoS) measurements can be converted into an object-fixed coordinate system consisting of vertical, longitudinal and transversal displacement components, which is complemented by metrics for the sensitivity and observability of displacements along the linear infrastructure (Chang et al., 2018). Infrastructure monitoring requires the assessment of spatial and temporal gradients that can damage infrastructures (Raspini et al., 2019; Barra et al., 2022; Zhang et al., 2025). The spatial gradient describes the change of the displacement between two points in space normalized by their distance, also called angular distortion, while the gradient velocity represents the change of the gradient over time (Ma et al., 2022; Daud et al., 2026). In practice, the spatial gradient is implicitly analysed, e.g. through profiles or visual analysis of displacement maps, or alternatively, the differential displacement velocity between two points is computed to identify the hazard at infrastructures (Qin et al., 2017; Chang et al., 2020; Wang et al., 2022). Chang et al. (2016) proposed a method to detect spatiotemporal displacement anomalies at railway tracks which classifies the temporal displacement behaviour of differential displacement time series between neighbouring PS pixels. However, the approach requires the final displacement time series to estimate both, the temporal and spatial gradients, which is connected to high computational costs. In this paper, we propose a novel approach that estimates the differential displacement velocity directly from the wrapped phases, to derive the spatial gradient velocity in a computationally light manner.

3. Methodology

The goal of our proposed method is to estimate the spatial displacement gradient velocities along the linear infrastructure from the SAR images. We limit our analysis to the linear infrastructure and directly estimate the spatial gradients from the wrapped interferometric phases. This approach does not require phase unwrapping and explicit estimation of the atmospheric effect. The gradients are estimated between neighbouring points whose phase difference cancels the atmospheric phase contribution for close-by pixels such that the atmospheric effect is negligible.
With our method, we perform a single-look analysis to avoid incoherent averaging of the pixels on the linear infrastructure through multilooking. Nevertheless, the spatial distribution of the coherent pixels can vary significantly along the linear infrastructure. Therefore, we apply a sampling strategy with grid cells which eases the interpretation of the estimated gradients along the linear infrastructure. We assume that the displacement signal is spatially correlated and, hence, we can use a regular grid that is computed along the linear infrastructure to aggregate coherent pixels within each grid cell.
The input to our method are the co-registered and geocoded Single-Look Complex (SLC) stack and a line from Geographic Information System (GIS) data with the centre coordinates representing the linear infrastructure, here referred to as infrastructure line. The map coordinates of each pixel in the image and of the infrastructure line has to be known in order to find pixels on the infrastructure and to construct a local coordinate system. The output of our method are the differential displacement velocities between neighbouring grid cells from which the spatial gradient velocities are computed.

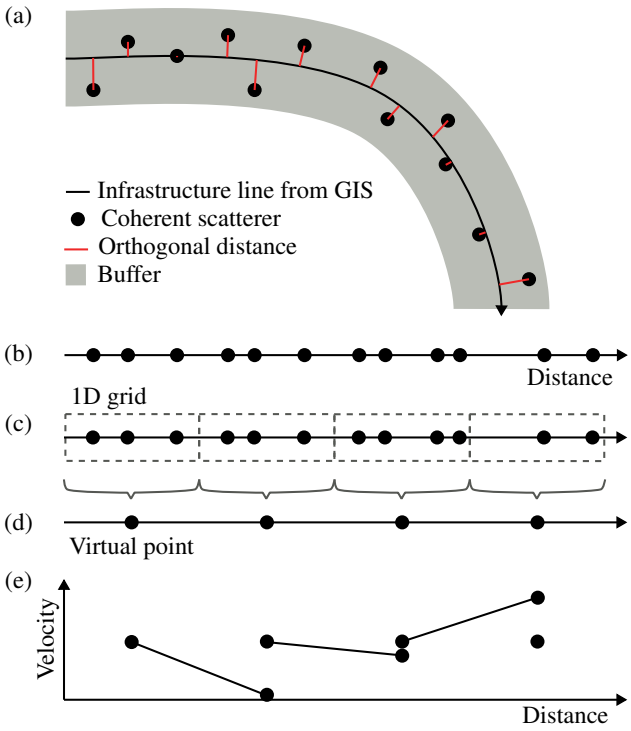

Figure 1. Illustration of the processing steps for the projection of the coherent points to the infrastructure line (a-b), to form a regular 1D grid (c), where each grid cells is represented by a virtual point (d). The results are the differential displacement velocities (e) or, if normalized by the distance, the spatial gradient velocities.

3.1 Pixel Selection

We select pixels at the linear infrastructure from which the spatial gradients can be computed. The position of the linear infrastructure in the radar image can be inferred from GIS data. If we assume that the geolocation of the coregistered image stack is accurate and the terrain is flat at the linear infrastructure, we can match the map coordinates of the infrastructure line with the map coordinates of the pixels in the radar image. A buffer is created along the infrastructure line in the radar image to mask the pixels belonging to the infrastructure.
Within the infrastructure mask, pixels which show a coherent scattering behaviour during the whole study period are selec-

ted (Figure 1a). Coherent pixels can comprise PS and Distributed Scatterer (DS) pixels, each requiring dedicated selection methods, e.g. amplitude stability analysis (Ferretti et al., 2001), phase noise estimation (Hooper et al., 2007), or phase linking (Guarnieri and Tebaldini, 2008; Ferretti et al., 2011). The choice of the pixel selection method is not specific to our proposed method.

3.2 Local Coordinate System

The gradients are analysed in a local coordinate system following the shape of the linear infrastructure. The selected coherent pixels are projected orthogonally onto the infrastructure line and the distance along the infrastructure relative to a starting point is computed. The infrastructure line comprises a series of straight lines, thereby enabling the projection of the points. The local coordinate system is one-dimensional and is given by the distance along the infrastructure (Figure 1b). The direction orthogonal to the infrastructure line is not required for our task as the coherent points are already selected with the buffer around the infrastructure line. An equidistant grid is computed along the infrastructure line and the coherent pixels are assigned to the grid cells (Figure 1c). Empty grid cells are discarded. Each grid cell is represented by its centre point, which is called virtual point hereafter.

3.3 Spatial Gradient Velocity Estimation

The spatial gradient velocity is estimated from arcs that connect two neighbouring grid cells. The arcs are not redundant. Nevertheless, reliability is increased by the aggregation of all pixel information within each grid cell into a virtual point, which thus serves as a cell representation (Figure 1d). Outlier checks could be applied on the coherent pixels before aggregating them. The virtual points are connected by arcs along the transport infrastructure which eases the interpretation of the gradients.
First, the interferometric phases of each coherent pixel are computed from the interferogram network. The phase ϕ in interferogram i of the virtual point p is the argument of the sum of complex phasors of all points in the grid cell Q

$$\phi_p^i = \angle \left(\sum_{q \in Q} e^{j\phi_q^i} \right) \tag{1}$$

where $\angle(\cdot)$ denotes the phase of a complex number. Then the arc phase φ is given by

$$\varphi^i = \angle \left(e^{j\phi_{Q_1}^i} \cdot e^{-j\phi_{Q_2}^i} \right) \tag{2}$$

ensuring that the gradient is always computed in the same direction along the infrastructure as grid cell Q_1 is closer to the starting point of the infrastructure line than Q_2.
We model the phase contributions in the arc phase with the differential mean displacement velocity Δv (Figure 1e), and with the difference in the Digital Elevation Model (DEM) error Δh. We choose the linear model for the displacement because we assume that the displacement signal is spatially correlated. For each arc, we estimate the two parameters by maximizing the temporal coherence from M interferograms

$$\underset{\Delta v, \Delta h}{\operatorname{argmax}} \, \hat{\gamma}_{\text{arc}} = \frac{1}{M} \cdot \left| \sum_{i=1}^{M} e^{j\varphi_{\text{res}}^i(\Delta v, \Delta h)} \right| \tag{3}$$

which measures the model fit based on the phase residuals φ_{res}^i. The phase residuals are computed based on the model for the displacement gradient and DEM error

$$\varphi_{\text{res}}^i(\Delta v, \Delta h) = \varphi^i - \frac{4\pi}{\lambda} \left(B_t^i \Delta v + \frac{B_\perp^i}{r \sin\theta} \Delta h \right) \tag{4}$$

where λ is the radar wavelength, $B_\perp^i$ is the perpendicular baseline, r is the average distance between the sensor and the point, θ is the average local incidence angle of the arc, and B_t^i is the temporal baseline (Ferretti et al., 2000). Low-quality estimates can be removed by a threshold on the temporal coherence $\hat{\gamma}_{\text{arc}}$. Finally, the spatial gradient velocity β is computed

$$\beta = \frac{\Delta v}{d} \tag{5}$$

using the distance d between the two grid cell centres.

4. Experiments

4.1 Study Area and Datasets

We selected a study area in Germany close to the city Düren depicted in Figure 2. The study area covers two open-pit mines, Hambach and Inden, and is characterized by subsidence related to the mining activities (Tang et al., 2020). Several highways and railways pass the study area of which two are selected for the validation of our method. The selected highway and railway sections cover 14 km and 12 km, respectively.
Two datasets from Sentinel-1 and TerraSAR-X are chosen. The C-band sensor from Sentinel-1 has a medium spatial resolution of 5 m×20 m, while the X-band sensor of TerraSAR-X has high spatial resolution of 3 m×3 m in range and azimuth, respectively. Both image stacks from Sentinel-1 and TerraSAR-X are separately coregistered with Gamma software (Wegmüller et al., 2016) using the Shuttle Radar Topography Mission (SRTM) DEM. The image stack of Sentinel-1 spans the period from 04-01-2021 until 30-12-2021 with 58 images from descending track. The image stack of TerraSAR-X contains 29 images from descending track in the period from 06-01-2021 until 04-01-2022. The study area covered by both sensors (red rectangle in Figure 2b) has an extent of about 12 km×8 km. The LoS viewing direction of the two sensors are almost the same for our study area with an incidence angle of around 35° which allows the direct comparison of the displacement results in LoS.

4.2 Processing Parameters

We processed the two image stacks from Sentinel-1 and TerraSAR-X independently using the same parameters for our method. Moreover, the linear infrastructures, railway and highway, are processed independently. We create a mask in the radar image coordinate system from the OpenStreetMap (OSM) lines of the linear infrastructure by buffering the line with 20 m on each side. The buffered line is subdivided into grid cells with a width of 200 m. Without loss of generality, we select PS pixels using the Temporal Phase Coherence (TPC) approach (Zhao and Mallorqui, 2019) and select coherent pixels within each mask which exceed a TPC value of 0.8. Using TPC compared to other commonly used methods like the amplitude dispersion (Ferretti et al., 2001) has the advantage that the phase noise is directly assessed and leads to a low false-positive detection rate (Zhao and Mallorqui, 2019). Therefore, we do not apply any further outlier checking before aggregating the coherent pixels to a virtual point in each grid cell. Arcs with a temporal coherence below 0.6 are removed.

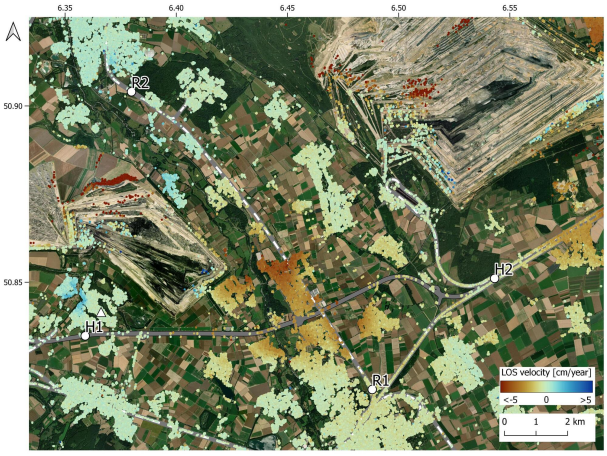

(a) Sentinel-1.

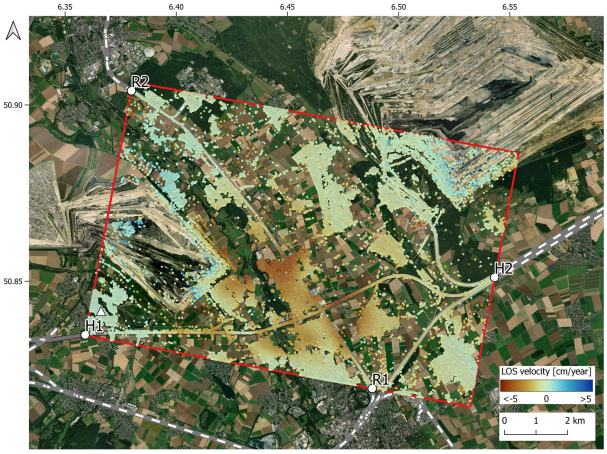

(b) TerraSAR-X.

Figure 2. LoS velocity maps estimated from MTInSAR over the study area in Germany with the two open-pit mines Hambach and Inden with the spatial reference point depicted by the white triangle. The study area covers several railway tracks and highways. The start and end points of the railway and highway segments analysed in our experiments (see Figure 3) are indicated by R1-R2 and H1-H2, respectively. Background image: ©ESRI.

4.3 Validation Strategy

We verify the spatial gradients estimated with our proposed method compared to a state-of-the-art MTInSAR method implemented in the SARvey open-source research software (Piter et al., 2024, 2025). With this conventional approach to linear infrastructure monitoring, we estimate the velocity map and the displacement time series for the whole study area. For MTInSAR, we estimate the TPC from a single-reference interferogram network and use the same threshold of 0.8 to select coherent pixels as it is applied for our proposed method. A two-step approach is chosen which first estimates the atmospheric effect from the first-order points and then densifies the set of second-order points. The phases are unwrapped temporally and spatially, the latter using the Phase Unwrapping MAx-flow (PUMA) method (Bioucas-Dias and Valadao, 2007; Boykov and Kolmogorov, 2004).

We compare the MTInSAR results from the conventional method with our proposed approach. On the one hand, we perform a visual assessment of the results on the level of the displacement velocities, i.e. we integrate the gradients of the arcs from our method to the velocity at each grid cell. For this, we assume that one grid cell is stable to serve as a reference and integrate the gradients of the connected arcs. Multiple reference cells are needed if grid cells are not connected.

On the other hand, we compare the results on the level of the differential displacement velocities. For this purpose, we also derive the differential displacement velocities from the mean velocity map of the MTInSAR method. We use the same grid cells and arcs as in the proposed method to average the velocities of all coherent pixels inside a grid cell and compute the velocity difference between neighbouring cells. Finally, the Root Mean Square Error (RMSE) is derived from K arcs between the grid cells along the linear infrastructure

$$RMSE_{\text{arc}} = \sqrt{\frac{1}{K}\sum_{i=1}^{K}(\Delta\bar{v}_i - \Delta v_i)^2}. \tag{6}$$

with the differential displacement velocities from the conventional MTInSAR denoted by $\Delta\bar{v}$ and from the proposed method by Δv. This metric, however, does not reflect how well the proposed method captures the details of the velocity profile along the linear infrastructure. Therefore, we assess how the estimated spatial gradients agree with the displacement velocities at the level of the coherent pixels resulting from MTInSAR. We formulate this assessment as a regression analysis, in which the fit of the gradient velocity β_i of the i-th arc is evaluated against the velocity estimates v_q of all coherent points from the two adjacent grid cells Q_1 and Q_2 at distances d_q

$$r_q = d_q\beta_i - v_q \tag{7}$$

yielding the residual velocity r_q of the coherent pixel q. We compute the RMSE over all arcs

$$RMSE_{\text{points}} = \sqrt{\frac{1}{\tilde{N}}\sum_{i=1}^{K}\left(\sum_{q\in Q_1}(r_q - \bar{r}_i)^2 + \sum_{q\in Q_2}(r_q - \bar{r}_i)^2\right)} \tag{8}$$

with the mean of the residuals $\bar{r}_i$ per arc. The total number of residuals $\tilde{N}$ used in this calculation depends on the number of coherent pixels N_i in the two grid cells Q_1 and Q_2 adjacent to arc i

$$\tilde{N} = \sum_{i=1}^{K} N_{i,Q_1} + N_{i,Q_2}. \tag{9}$$

The assessment is done for each sensor and each linear infrastructure separately.

4.4 Results and Discussion

The displacement maps are shown in Figure 2 with the LoS mean velocity estimated from Sentinel-1 and TerraSAR-X images. The same overall displacement signal has been retrieved from the data of both sensors showing a diverse displacement field related to subsidence in the urban areas and on the linear infrastructures with a maximum velocity of about 4.5 cm/year away from the satellite and displacement related to uplift at the open-pit mines and in their vicinity. While a dense coverage of the railway and highway has been achieved in the TerraSAR-X results, the linear infrastructures are sparsely covered in the Sentinel-1 results. These displacement maps, being a standard product of MTInSAR, show the overall displacement signal.

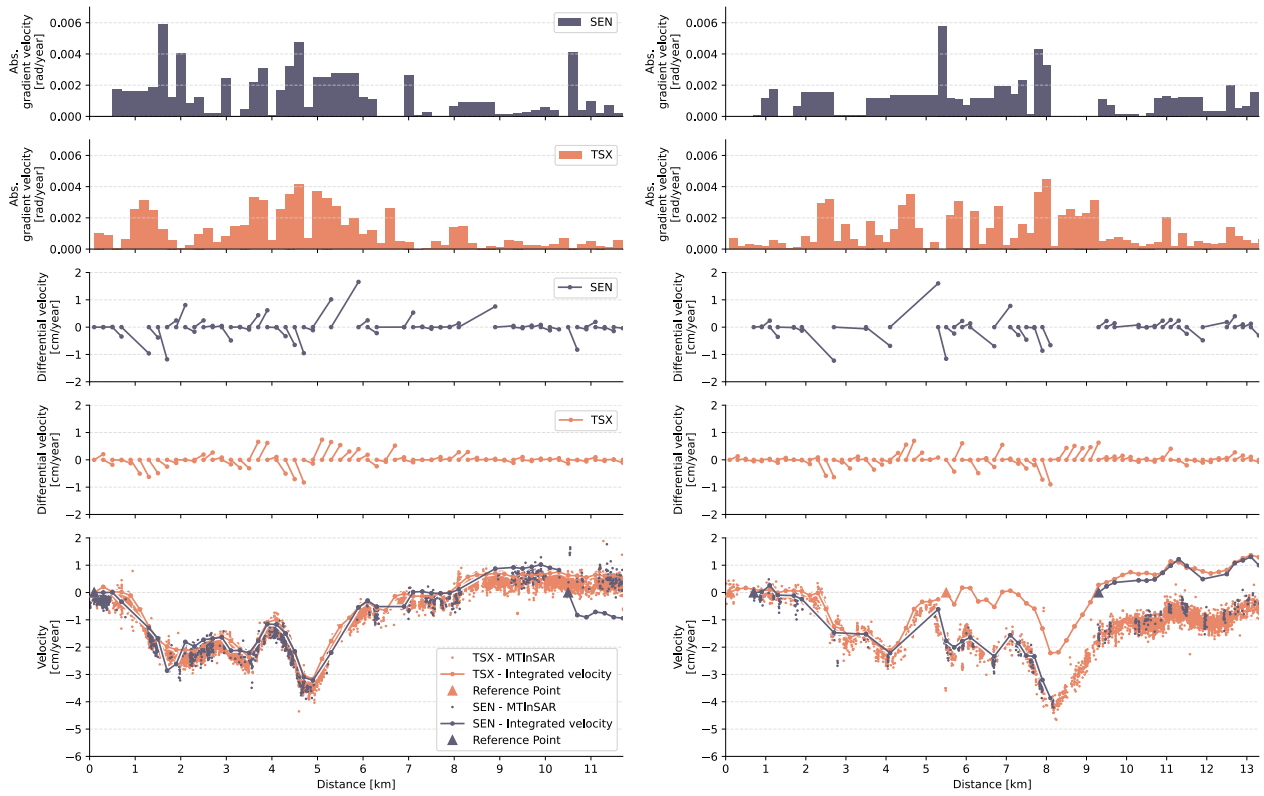

(a) Railway from R1 to R2.

(b) Highway from H1 to H2.

Figure 3. Absolute spatial gradient velocities (first and second row) along the linear infrastructures estimated from Sentinel-1 (grey) and TerraSAR-X images (orange). The differential displacement velocities between the grid cells are shown for each arc (third and fourth row). The first grid cell of an arc serves as reference and is set to zero, while the displacement velocity of the second grid cell displays the displacement velocity of the arc relative to the first grid cell. Empty grid cells in the Sentinel-1 results lead to different arc length compared to the TerraSAR-X result. The velocities at the grid cells (bottom) result from integrating the differential displacement velocities along the linear infrastructure relative to the first grid cell, depicted by a triangle. In case of missing arcs, a new reference point is deployed. The velocities of coherent points derived from conventional MTInSAR analysis are provided for comparison.

However, their interpretability for hazard assessment is limited especially for the linear infrastructures with their narrow shape.

The results of the linear infrastructure-oriented analysis proposed in this paper are shown in Figure 3 for the railway and highway segment. The results are presented in three ways: the absolute values of the spatial gradient velocities (first and second row), the differential velocities between two arcs (third and fourth row), and integrated velocities in comparison to the MTInSAR velocities (bottom row). The grid cells derived from TerraSAR-X data are all filled with coherent pixels, thus, all arcs have the same length. Moreover, it was possible to estimate the gradient for all arcs, except for one arc at the highway, leading to a continuous representation of the spatial gradient velocity along the two linear infrastructures. Although not all grid cells derived from the Sentinel-1 data are filled with coherent points, the gradient was estimated for all, except for two arcs. A few arcs are longer than the regular sampling distance of 200 m as a consequence of the empty grid cells. This leads to an undersampling of the displacement gradients along the linear infrastructure, which is, however, not due to the proposed methodology, but depends on the availability of coherent pixels.
The primary outcomes of our approach are the spatial gradient velocities along linear infrastructures (first and second row of Figure 3). The retrieved gradient velocities demonstrate consistency with the MTInSAR velocity profiles, but differences between the results from the two sensors are apparent. These differences can be attributed to the spatial resolution and the availability of coherent points. For example, the high gradient velocities along the railway at 4 km to 6 km distance are consistently retrieved from Sentinel-1 and TerraSAR-X images. However, the gradient velocities along the highway at 8 km to 9.5 km are estimated from TerraSAR-X but not from Sentinel-1 due to insufficient number of coherent pixels.
Another product of the proposed approach are the differential displacement velocities (third and fourth row of Figure 3). To enhance the readability of the differential velocities, the first point of each arc is set as a local reference, while the second point is representing the velocity difference away or towards the sensor. Obviously, the overall displacement signal is not directly visible from the differential velocities, however, local differences in the displacement at segments of the linear infrastructure are highlighted. Finally, the differential velocities from the proposed approach are integrated relative to a reference grid cell in order to compare it with the velocity profiles from MTInSAR (bottom row of Figure 3). In case of a missing arc, a new reference point is set, which happens twice in the Sentinel-1 and once in the TerraSAR-X results. This representation allows to assess the global displacement signal similar to the displacement maps in Figure 2 and might be more familiar to the reader. The velocities resulting from integration

This contribution has been peer-reviewed. The double-blind peer-review was conducted on the basis of the full paper.
https://doi.org/10.5194/isprs-annals-XI-3-2026-447-2026 | © Author(s) 2026. CC BY 4.0 License.

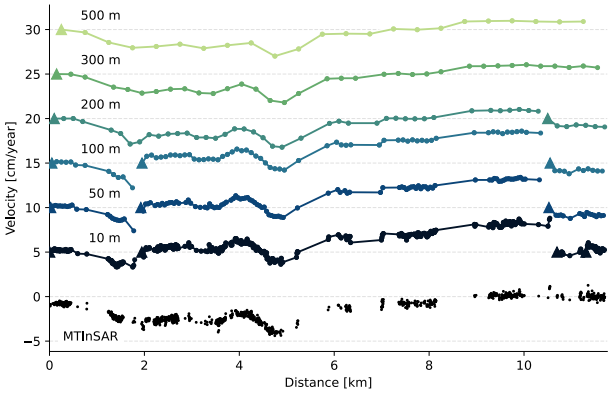

Figure 4. Integrated velocities along railway segment derived from Sentinel-1 data for different grid sizes.

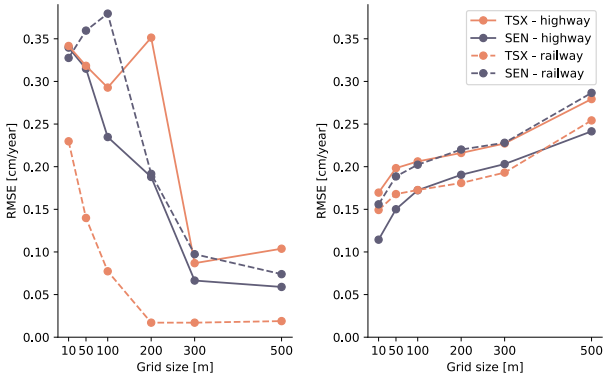

(a) $RMSE_{\text{arc}}$. (b) $RMSE_{\text{points}}$.

Figure 5. RMSE between MTInSAR results and proposed approach for different grid sizes.

are not the output of our method, because the integration will lead to drift which increases along the velocity profile. The results from our method and from MTInSAR follow the same overall displacement pattern for both Sentinel-1 and TerraSAR-X. From the figure, only small differences are visible resulting from undersampling of the displacement signal through a grid cell size of 200 m such that the averaging effect of the sampling becomes apparent. At the railway, there is a larger discrepancy between Sentinel-1 and TerraSAR-X results around kilometres 10 to 11. Notably, the velocity of coherent pixels derived from MTInSAR varies along the profile in the range of 0.5 and 1 cm/year. In contrast, the velocities from our approach do not show any variation as the phases are averaged in the beginning on the grid cell level.

The impact of the chosen grid size on the integrated velocities retrieved with our proposed approach is shown in Figure 4 with grid sizes in the range of 10 m to 500 m. Two effects can be observed. Firstly, the displacement velocities become smoother with increasing grid size. This effect is expected because the interferometric phases of all pixels inside each grid cell are averaged. Secondly, as the grid size decreases, there is an increase in the number of arcs whose large phase noise prevents the estimation of the displacement velocity. The use of a smaller grid size amplifies the impact of noise from incoherent pixels, whereas a larger grid size smooths the differential velocities which prevents the assessment of local displacement anomalies.

The comparison between the MTInSAR results and the proposed approach is shown in Figure 5. The results on the level of the arcs (Figure 5a) correspond more closely with increasing grid size. This demonstrates that the long-wavelength displacement signals can be better captured, while the high RMSE at short arcs reflect the variability of the displacement velocities from individual coherent pixels along the velocity profile of the infrastructure. Moreover, the L-shaped RMSE-curves indicate that local displacement signals have a minor impact on the differential velocities of grid sizes larger than 300 m. An exception is the RMSE-curve corresponding to railway observed by TerraSAR-X, which in general shows significantly lower RMSE values for all grid sizes and exhibits a bend in the L-shaped curve already at 200 m grid size. The low RMSE for the railway depicted in TerraSAR-X images could result from the high spatial sampling of the displacement due to the high number of and homogeneously distributed coherent pixels at the railway.

The comparison of the spatial gradient from the proposed approach with the velocities at the coherent points from MTInSAR is shown in Figure 5b. All RMSE-curves (rail- and highway, from both sensors) exhibit a similar behaviour as they grow with increasing grid size. It confirms that less velocity variations are captured with larger grid sizes. The values range from 0.11 cm/year to around 0.30 cm/year. Interestingly, there is only a slight increase in the RMSE of less than 0.05 cm/year between grid sizes 50 m to 300 m, while for the same grid sizes the RMSE on the arc level decreases drastically (difference up to -0.25 cm/year, Figure 5a). This indicates that the velocities estimated from MTInSAR show themselves a variation of around 0.2 cm/year along the linear infrastructures.

Discrepancies between our approach and MTInSAR could be explained by the different processing strategies. However, they cannot be assigned to one method because a ground-truth is not available for the study area. In our approach, the pixels in the neighbourhood of the linear infrastructure do not have an effect on the estimation, whereas the phase unwrapping and time series retrieval in MTInSAR depend on the distribution and quality of all pixels in the study area. Averaging the phases of the coherent pixels within each cell in our approach can either reduce or increase the impact of individual pixels depending on the total number of pixels in the cell. Another reason for the differences could be the linear displacement model which is assumed in our approach but is not appropriate for pixels with a non-linear displacement which the MTInSAR method is able to retrieve.

Our method uses a regular grid spacing which works well for the homogeneously distributed coherent pixels from TerraSAR-X, but might not be optimal for the heterogenous spatial distribution of coherent pixels in Sentinel-1 images. The regular grid spacing could segregate coherent pixels, which are spatially clustered, into grid cells with only one or few pixels. An unsupervised clustering approach could help to group pixels by their spatial distribution.

5. Conclusion

In this paper, we introduced a new concept for linear infrastructure monitoring. The approach estimates the spatial gradient velocities directly from the wrapped interferometric phases in contrast to MTInSAR which is commonly used for this task. Our methodology works for both high and medium spatial resolution SAR images from TerraSAR-X and Sentinel-1, but provides opportunities for large scale linear infrastructure monitoring if applied on Sentinel-1 images. We showed that al-

This contribution has been peer-reviewed. The double-blind peer-review was conducted on the basis of the full paper.
https://doi.org/10.5194/isprs-annals-XI-3-2026-447-2026 | © Author(s) 2026. CC BY 4.0 License.

though a larger grid size leads to smoothing of the displacement velocities, the success rate of the displacement velocity estimation increases with increasing grid size. The experiments demonstrated that regional displacement signals can be effectively estimated with our method from Sentinel-1 images to leverage the wide-area coverage of the sensor. In future work, we will focus on the identification of temporal anomalies to complement the spatial gradients. Moreover, we will apply our method to larger areas and combine the LoS gradients from different orbit directions in order to decompose the signal into an object-fixed coordinate system.

Acknowledgements

The results contain modified Copernicus data provided by the European Space Agency (ESA). TerraSAR-X images are copyright of German Aerospace Center (DLR) provided under the proposal motagh_GEO1916. The figures are created with QGIS (QGIS Development Team, 2025), Python and the Scientific Colour Maps (Crameri et al., 2020).

References

Barra, A., Reyes-Carmona, C., Herrera, G., Galve, J. P., Solari, L., Mateos, R. M., Azañón, J. M., Béjar-Pizarro, M., López-Vinielles, J., Palamà, R., Crosetto, M., Sarro, R., Cuervas-Mons, J., Monserrat, O., 2022. From satellite interferometry displacements to potential damage maps: A tool for risk reduction and urban planning. *Remote Sensing of Environment*, 282, 113294.

Bernhard, P., Haener, D., Frey, O., 2024. Detection of Railway Track Anomalies Using Interferometric Time Series of TerraSAR-X Satellite Radar Data. *IEEE Journal of Selected Topics in Applied Earth Observations and Remote Sensing*, 17, 11750–11760.

Bioucas-Dias, J. M., Valadao, G., 2007. Phase Unwrapping via Graph Cuts. *IEEE Transactions on Image Processing*, 16(3), 698–709.

Boykov, Y., Kolmogorov, V., 2004. An experimental comparison of min-cut/max-flow algorithms for energy minimization in vision. *IEEE Transactions on Pattern Analysis and Machine Intelligence*, 26(9), 1124–1137.

Chang, L., Dollevoet, R. P., Hanssen, R. F., 2016. Nationwide railway monitoring using satellite SAR interferometry. *IEEE Journal of Selected Topics in Applied Earth Observations and Remote Sensing*, 10(2), 596–604.

Chang, L., Dollevoet, R. P., Hanssen, R. F., 2018. Monitoring line-infrastructure with multisensor SAR interferometry: Products and performance assessment metrics. *IEEE Journal of Selected Topics in Applied Earth Observations and Remote Sensing*, 11(5), 1593–1605.

Chang, L., Hanssen, R., 2015. Detection of permafrost sensitivity of the Qinghai–Tibet railway using satellite radar interferometry. *International Journal of Remote Sensing*, 36(3), 691–700.

Chang, L., Sakpal, N. P., Elberink, S. O., Wang, H., 2020. Railway Infrastructure Classification and Instability Identification Using Sentinel-1 SAR and Laser Scanning Data. *Sensors*, 20(24), 7108.

Crameri, F., Shephard, G. E., Heron, P. J., 2020. The misuse of colour in science communication. *Nature Communications*, 11(1), 5444.

Crosetto, M., Solari, L., Mróz, M., Balasis-Levinsen, J., Casagli, N., Frei, M., Oyen, A., Moldestad, D. A., Bateson, L., Guerrieri, L., Comerci, V., Andersen, H. S., 2020. The Evolution of Wide-Area DInSAR: From Regional and National Services to the European Ground Motion Service. *Remote Sensing*, 12(12), 2043.

Daud, N., Dasho, O., Shirzaei, M., 2026. Probabilistic modeling of InSAR-derived land subsidence hazard in New York City for transportation infrastructure damage risk assessments. *International Journal of Applied Earth Observation and Geoinformation*, 146, 105118.

Ferretti, A., Fumagalli, A., Novali, F., Prati, C., Rocca, F., Rucci, A., 2011. A new algorithm for processing interferometric data-stacks: SqueeSAR. *IEEE Transactions on Geoscience and Remote Sensing*, 49(9), 3460–3470.

Ferretti, A., Prati, C., Rocca, F., 2000. Nonlinear subsidence rate estimation using permanent scatterers in differential SAR interferometry. *IEEE Transactions on Geoscience and Remote Sensing*, 38(5), 2202–2212.

Ferretti, A., Prati, C., Rocca, F., 2001. Permanent scatterers in SAR interferometry. *IEEE Transactions on Geoscience and Remote Sensing*, 39(1), 8–20.

Guarnieri, A. M., Tebaldini, S., 2008. On the exploitation of target statistics for SAR interferometry applications. *IEEE Transactions on Geoscience and Remote Sensing*, 46(11), 3436–3443.

Gürboğa, Ş., Çomut, F. C., Lyu, S., Motagh, M., Thu, K. S., Karadağlar, M., 2025. Heterogeneous rupturing and barrier mechanism during the 2025 Mw7.7 Myanmar earthquake. *Scientific Reports*, 15(1), 41144.

Haghighi, M. H., Motagh, M., 2024. Uncovering the impacts of depleting aquifers: A remote sensing analysis of land subsidence in Iran. *Science Advances*, 10(19), eadk3039.

Hanssen, R. F., 2001. *Radar Interferometry: Data Interpretation and Error Analysis*. 2, Springer Science & Business Media.

Hooper, A., Segall, P., Zebker, H., 2007. Persistent scatterer interferometric synthetic aperture radar for crustal deformation analysis, with application to Volcán Alcedo, Galápagos. *Journal of Geophysical Research: Solid Earth*, 112(B7).

Kalia, A. C., Frei, M., Lege, T., 2017. A Copernicus downstream-service for the nationwide monitoring of surface displacements in Germany. *Remote Sensing of Environment*, 202, 234–249.

Ma, P., Zheng, Y., Zhang, Z., Wu, Z., Yu, C., 2022. Building risk monitoring and prediction using integrated multitemporal InSAR and numerical modeling techniques. *International Journal of Applied Earth Observation and Geoinformation*, 114, 103076.

Macchiarulo, V., Milillo, P., Blenkinsopp, C., Giardina, G., 2022. Monitoring deformations of infrastructure networks: A fully automated GIS integration and analysis of InSAR time-series. *Structural Health Monitoring*, 14759217211045912.

Mora, O., Mallorqui, J., Broquetas, A., 2003. Linear and nonlinear terrain deformation maps from a reduced set of interferometric SAR images. *IEEE Transactions on Geoscience and Remote Sensing*, 41(10), 2243–2253.

Morishita, Y., 2021. Nationwide urban ground deformation monitoring in Japan using Sentinel-1 LiCSAR products and LiCSBAS. *Progress in Earth and Planetary Science*, 8(1), 6.

Orellana, F., Delgado Blasco, J. M., Foumelis, M., D’Aranno, P. J., Marsella, M. A., Di Mascio, P., 2020. DInSAR for Road Infrastructure Monitoring: Case Study Highway Network of Rome Metropolitan (Italy). *Remote Sensing*, 12(22), 3697.

Piter, A., Haghighi, M. H., FERN.Lab, Motagh, M., 2025. SARvey - survey with SAR v1.2.0.

Piter, A., Haghighi, M. H., Motagh, M., 2024. Challenges and Opportunities of Sentinel-1 InSAR for Transport Infrastructure Monitoring. *PFG – Journal of Photogrammetry, Remote Sensing and Geoinformation Science*, 92(5), 609–627.

QGIS Development Team, 2025. QGIS Geographic Information System. QGIS Association.

Qin, X., Liao, M., Zhang, L., Yang, M., 2017. Structural Health and Stability Assessment of High-Speed Railways via Thermal Dilation Mapping With Time-Series InSAR Analysis. *IEEE Journal of Selected Topics in Applied Earth Observations and Remote Sensing*, 10(6), 2999–3010.

Raspini, F., Bianchini, S., Ciampalini, A., Del Soldato, M., Montalti, R., Solari, L., Tofani, V., Casagli, N., 2019. Persistent Scatterers continuous streaming for landslide monitoring and mapping: the case of the Tuscany region (Italy). *Landslides*, 16(10), 2033–2044.

Tang, W., Motagh, M., Zhan, W., 2020. Monitoring active open-pit mine stability in the Rhenish coalfields of Germany using a coherence-based SBAS method. *International Journal of Applied Earth Observation and Geoinformation*, 93, 102217.

Van Leijen, F. J., 2014. Persistent scatterer interferometry based on geodetic estimation theory. PhD thesis, Technical University Delft.

Wang, R., Yang, M., Dong, J., Liao, M., 2022. Investigating deformation along metro lines in coastal cities considering different structures with InSAR and SBM analyses. *International Journal of Applied Earth Observation and Geoinformation*, 115, 103099.

Wegmüller, U., Werner, C., Strozzi, T., Wiesmann, A., Frey, O., Santoro, M., 2016. Sentinel-1 Support in the GAMMA Software. *Procedia Computer Science*, 100, 1305–1312.

Zhang, X., Chen, L., Yin, K., Zhao, Z., Chen, Q., Zhu, S., Xia, J., 2025. Fragility and vulnerability curves of masonry buildings on slow-moving landslides: A comparative study on intensity parameters from MT-InSAR. *Engineering Geology*, 355, 108212.

Zhao, F., Mallorqui, J. J., 2019. A Temporal Phase Coherence Estimation Algorithm and Its Application on DInSAR Pixel Selection. *IEEE Transactions on Geoscience and Remote Sensing*, 57(11), 8350–8361.